

Internal jet interactions in a fluidic oscillator at low flow rate

Mehmet N. Tomac · James W. Gregory

Received: 8 February 2014 / Revised: 27 March 2014 / Accepted: 11 April 2014 / Published online: 1 May 2014
© Springer-Verlag Berlin Heidelberg 2014

Abstract This study focuses on the internal jet interactions and the oscillation mechanism of the feedback-free fluidic oscillator at low flow rate, corresponding to a Reynolds number of 1,350 (based on exit nozzle width and average exit velocity). Particle image velocimetry (PIV) was used in this study with a refractive index-matched fluid to minimize reflections that would otherwise occur at the fluid-acrylic interface in the test setup. A simple microphone-tube sensor configuration generated a reference signal, with a phase-averaging method based on each quarter period for velocity time history reconstruction. PIV results revealed the existence of a vortex of fluctuating size, shape, and strength on each side of the oscillator; and two transient vortices that are formed in the dome region of the oscillator by each of the jets once per period. The dome vortices periodically bifurcate each of the jets and transfer some of the kinetic energy of that jet to the opposing jet. This kinetic energy transfer mechanism dictates the dominance of either jet at the exit, and this mechanism repeats itself to sustain the oscillations created by the fluidic oscillator. At this flow rate, the two jets form a continuous mutual collision, and the jets are never completely cut off

from the exit. The oscillatory behavior at this flow rate is due to a complex combination of jet interactions and bifurcations, vortex–shear layer interactions, vortex–wall interactions, and saddle point formations.

1 Introduction

Characterization of fluidic oscillators is crucial since fluidic oscillators are promising devices for various engineering applications, and there is an increased interest in flow control community to use them as flow control actuators. Wall-attachment-type and jet interaction-type fluidic oscillators are the two main types of the fluidic oscillators (Raghu 2013; Gregory and Tomac 2013). Wall-attachment fluidic oscillators have been extensively studied since the 1960s (e.g., Booth 1962; Spyropoulos 1964; Lush 1968; Gaylord and Carter 1969; Tesař and Bandalusena 2011; Bobusch et al. 2013; Tesař et al. 2013). However, jet interaction fluidic oscillators are relatively new, and more study is required in order to characterize and understand the operating mechanism of this type of fluidic oscillator. These fluidic oscillators are a very special case in the fluidic oscillator family, and its mode of operation is quite different from the standard wall-attachment-type fluidic oscillators with feedback channels. However, absence of diffusers inhibits a reasonable pressure recovery for the jet interaction fluidic oscillators and constricts their usage to applications in which efficiency is not the primary objective.

One of the pioneer designs of jet interaction-type fluidic oscillator is the feedback-free fluidic oscillator patented by Bowles Fluidics Corporation (Srinath and Koehler 2001; Raghu 2001). This design consists of two internal jets

Electronic supplementary material The online version of this article (doi:10.1007/s00348-014-1730-8) contains supplementary material, which is available to authorized users.

M. N. Tomac
Department of Mechanical Engineering, Abdullah Gul
University, 38039 Kayseri, Turkey
e-mail: mehmet.tomac@agu.edu.tr

J. W. Gregory (✉)
Department of Mechanical and Aerospace Engineering, The
Ohio State University, 201 W. 19th Ave., Columbus, OH 43210,
USA
e-mail: gregory.234@osu.edu

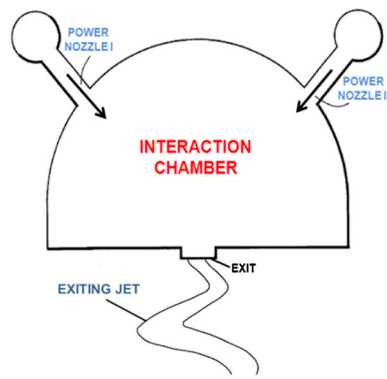


Fig. 1 Feedback-free fluidic oscillator design (Raghu 2001)

interacting in an interaction chamber as shown in Fig. 1. Jet interaction in the interaction chamber eventually leads to the self-sustained oscillation of the exiting jet. Gregory et al. (2005) visualized the internal jet interactions of the feedback-free fluidic oscillator by using pressure-sensitive paint (PSP) and flow visualization. They reported that two power jets create an unsteady shear layer by the collision, and this shear layer is driven by two counter-rotating side vortices. Gregory et al. (2007) also investigated a micro-scale version of the feedback-free fluidic oscillator to determine the characteristics of the oscillator for flow control applications. They reported that the variation of the frequency with the flow rate is linear, except one distinct inflection point. They concluded that different oscillation mechanisms might be responsible for different flow rates. Bidadi et al. (2011) used flow visualizations and numerical methods to extract the oscillation mechanism of the feedback-free fluidic oscillator and discussed that the unstable arrangement of jet interaction creates vortices leading to oscillatory behavior. Tomac and Gregory (2012) used particle image velocimetry (PIV) with a refractive index-matched sodium iodide solution to extract the dual jet interactions in the interaction chamber of the feedback-free fluidic oscillator. That study identified three distinct operating mechanisms in different flow rate regions, termed the low, transitional, and high flow rate regions. Observations of the internal flow in the high flow rate region revealed a flapping interaction of colliding jets similar to that studied by Denshchikov et al. (1978), where one jet is deflected toward the dome-shaped region while the other is deflected toward the nozzle exit. The low flow rate behavior was discussed by Tomac and Gregory (2013), while the present study focuses in increased detail on the jet interactions and oscillation mechanism of the feedback-free fluidic oscillators in the low flow rate region. The main aim of this investigation is to comprehend the detailed flow physics of dual jet interactions and bifurcations, the role of the side and dome vortices in the oscillation mechanism, the

interaction of the walls with the jets and the vortices, and the overall oscillation mechanism in the low flow rate region.

2 Experimental setup and data analysis

The feedback-free fluidic oscillator creates an oscillating jet as a result of fluid jet interactions in the dome-shaped internal chamber solely based on fluid dynamic principles. A refractive index-matched PIV technique together with a custom microphone-tube sensor setup was used to extract the phase-resolved internal velocity field of the oscillator. A phase-averaging method based on each quarter period is also discussed in detail.

2.1 Fluidic oscillator model

The fluidic oscillator model used for this investigation is a small design (12.5 mm width \times 15 mm length \times 1.5 mm depth) with an internal nozzle width of 1.70 mm and an exit nozzle width of 2 mm. Laser cutting, 3D printing and CNC manufacturing methods were considered for fabrication of the fluidic oscillator models, and laser cutting was chosen to be the optimum and the cleanest manufacturing solution. Furthermore, clear acrylic material was selected for optical access into the internal cavity. Laser-cut models were designed in three pieces since the laser only cuts two-dimensional sheets. An assembly of three laser-cut pieces constituted an oscillator model as seen in Fig. 2 (top and isometric views).

2.2 Refractive index-matched PIV technique

The PIV technique is an optical and non-intrusive experimental technique that provides instantaneous 2D or 3D velocity vectors of a flow field. Most PIV measurements are performed to obtain the external velocity fields over streamlined (i.e., airfoils) or bluff bodies (i.e., cylinders, spheres, etc.). In this present study, the PIV technique was used to extract the internal 2D velocity field of a fluidic oscillator.

Unpreventable reflections due to laser illumination dictated the use of a refractive index-matching fluid. A detailed list of refractive index-matching fluids used in experiments was tabulated by Budwig (1994). Out of all of the refractive index-matched fluids considered, a sodium iodide (NaI) solution was selected for this study. A 60 % NaI solution (by weight) was made with 5.5 kg of NaI added to 3.66 kg of distilled water to yield 5.5 L of solution with a density of 1,730 kg/m³. This solution has a refractive index around 1.5, very close to that of acrylic. The NaI solution was treated with the method suggested by

Fig. 2 CAD drawings of three-piece, laser-cut clear acrylic models

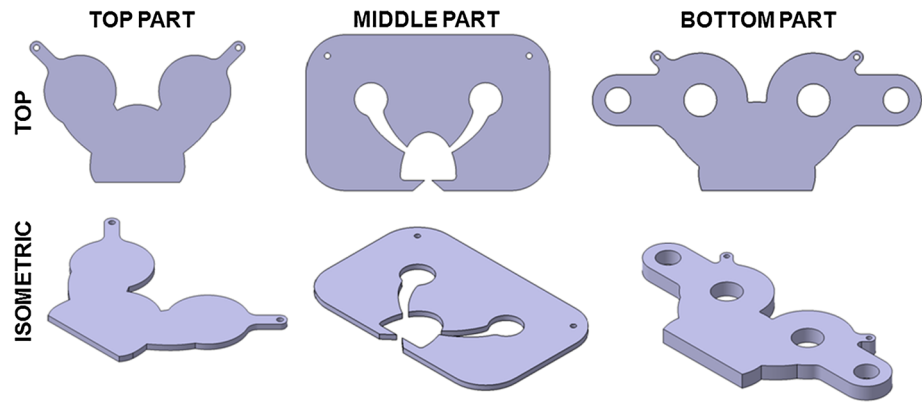
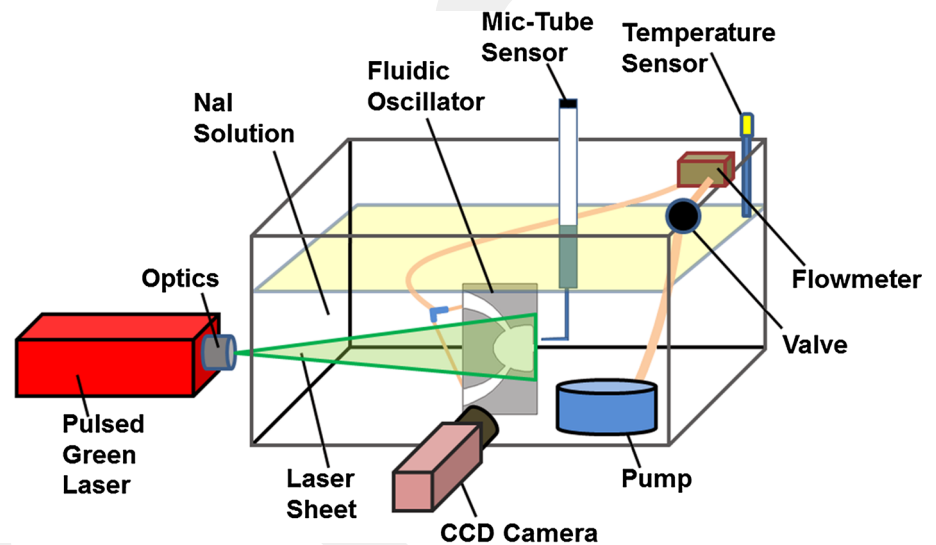


Fig. 3 Schematic of the refractive index-matched PIV setup



Uzol et al. (2002) and kept in a dark and oxygen-free container. Hollow glass spheres with density of $1,200 \text{ kg/m}^3$ and mean particle size of $10 \text{ }\mu\text{m}$ were added as tracer particles to the NaI solution. The maximum velocity error induced due to the density difference was calculated to be on the order of 10^{-4} m/s ; thus, any errors due to particle buoyancy are neglected in this study. In refractive index-matched PIV and frequency measurements, the uncertainty due to the effect of temperature on frequency measurements was calculated to be as high as $\pm 3.59 \%$ per $^\circ\text{C}$ change. In order to account for the effect of temperature in the calculations of density and viscosity of the NaI solution, temperature-based density and viscosity equations were obtained by polynomial fitting of the values provided by Zaytsev and Aseyev (1992).

The NaI solution was poured into an enclosure (150 mm width \times 300 mm length \times 200 mm depth), and then a closed loop fluid supply system for the fluidic oscillator was arranged with the help of a submerged 8.7 ft head ($\sim 26 \text{ kPa}$) magnetic-drive pump (Totalpond #MD11500).

This experimental setup is shown in Fig. 3. An Omega FLR1011ST flow meter with range of $\sim 3\text{--}33 \text{ mL/s}$ was used with a precision flow rate control needle valve. The flow meter was calibrated before the experimental trials with the help of a container, a stopwatch, and a graduated cylinder. The temperature of the NaI solution was measured with a K-type thermocouple (Omega Inc.) connected to NI USB-TC01 thermocouple measurement device and calibrated with a thermometer having $0.1 \text{ }^\circ\text{C}$ divisions (Kessler Corp. #2100-3). The microphone-tube sensor configuration was used for simultaneous frequency measurements. Microphone-tube raw voltage data were filtered and amplified by using a Krohn-Hite Corp. 3364 model analog filter. Two channels of the analog filter were used for band-pass filtering.

PIV measurements were performed with a 200 mJ double-pulsed Nd:YAG 532 nm laser (Quantel Evergreen 200) with a beam diameter less than 6.35 mm , a CCD camera (Cooke Corp. PCO 1600) with a macro lens (Sigma 105 mm , $1:2.8\text{D}$), a programmable timing unit (LaVison

External PTU V. 9.0), and laser sheet-forming optics (a spherical lens and a cylindrical lens) with a pinhole plate. The pinhole plate with 0.8-mm-diameter hole was used to reduce the laser sheet thickness to less than 1 mm since the depth of the fluidic oscillator is 1.5 mm. As shown in Fig. 3, fluidic oscillator was submerged and oriented in a vertical position, such that the exiting jet centerline was parallel to the ground and the cavity was perpendicular to the camera. For the flow rate discussed in this paper (2.8 mL/s), an inter-pulse delay (Δt) of 340 μ s was used. For this low flow rate, the pump was placed in a small container in the enclosure, and two holes were drilled on top of this small container allowing NaI to flow down into the container via these holes. By doing this, only surface fluid was allowed to flow into the container, and the surface level difference between the NaI solution enclosure and NaI solution container enhanced mixing. This simple setup increased the amount of hollow glass spheres observed in the interaction chamber of the fluidic oscillator.

LaVision's Davis 7.2 software was used for data acquisition and post-processing, in conjunction with LabView 8.6 and MATLAB R2011b. In Davis, each image pair was cross-correlated with multi-pass processing (64 \times 64 and 32 \times 32 window size) with 50 % overlap with the neighboring window and post-processed with the help of a median filter to remove spurious vectors. Furthermore, a 3 \times 3 Gaussian smoothing filter applied to the velocity vector fields. Simultaneous PIV and frequency measurements were made possible by externally triggering the Davis software, with the PIV recording controlled by a LabView Virtual Instrument (i.e., whenever the recording was started in LabView, a TTL trigger signal was sent to the Davis software from LabView to start PIV recording simultaneously). The microphone-tube sensor and flow meter were sampled at 5 kHz, and 600 PIV images were simultaneously captured at a rate of 3.75 Hz, yielding 160 s of total recording time. However, due to the fluctuations in flow rate and thus fluctuations in frequency, real-time readings from the microphone-tube sensor were not suitable for phase-locking, and a quarter period-based phase-averaging method was used to solve this problem (to be discussed in Sect. 2.4).

2.3 Microphone-tube sensor setup for frequency measurements in NaI solution

Although the use of NaI solution allowed obtaining distortion-free images for PIV velocity calculations, having a proper sensor for simultaneous frequency measurements in the NaI solution was problematic. Use of a hot-film sensor was impossible due to the electrochemical properties of the NaI solution. The use of a hydrophone was also not preferred due to the relatively large size of the sensor (thus

highly intrusive), higher cost, and higher frequency ranges than the frequency range (0–100 Hz) measured in the present study. Thus, a new sensor configuration was developed based on a condenser microphone (mic) in which the flow pulsations were transmitted by a compression fitting that separated the sodium iodide from an air-filled tube with the microphone at the other end. Figure 4 shows the schematic of the sensor setup. This sensor configuration consisted of a condenser microphone (Radio-shack 270-0092), Tygon tubing with inner diameter (ID) of 8 mm, a protective metal casing for the Tygon tubing, metal tubing with an outer diameter (OD) of 1 mm, a 6-V power supply, and BNC cable for transmitting the microphone signal. The conjunction regions between the condenser microphone and Tygon tubing, and also between the Tygon tubing and compression fitting cap, were sealed to ensure that the air inside the Tygon tubing was trapped between the liquid (NaI solution or water) and the condenser microphone. This sealing improved the signal-to-noise ratio (SNR) of the sensor setup. The condenser microphone is not waterproof; therefore, the length of Tygon tubing was selected to ensure that the liquid cannot reach the microphone sensor.

The amplitude of the measured oscillation phase signal tended to increase as the sensor was positioned closer to the oscillator exit. No detailed work was done to explain the operational mechanism of the microphone-tube sensor setup; however, it is thought that the condenser microphone measures the air pressure fluctuations caused by the motion of the liquid NaI solution in the small metal tubing that is exposed to the exiting jet. Furthermore, the free surface of the NaI solution in tubing is thought to act as a very

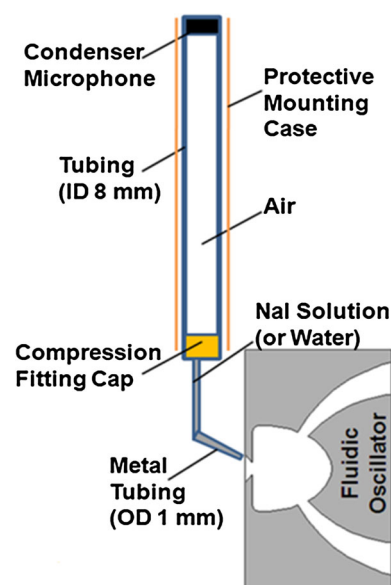


Fig. 4 Microphone-tube sensor configuration

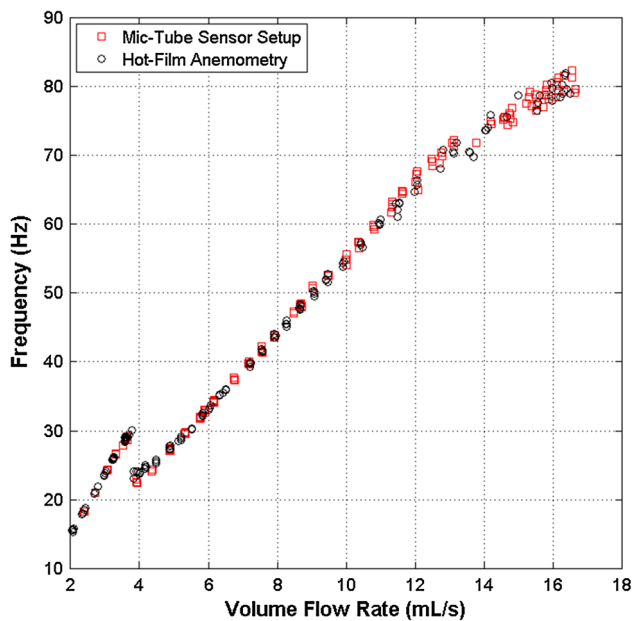


Fig. 5 Comparison of microphone-tube measurements with hot-film measurements (operated in water)

sensitive diaphragm that transfers any change to the air trapped inside the tubing. In order to test the accuracy of the new sensor setup, frequency measurements from the microphone-tube sensor were compared with those from hot-film anemometry. Both sensor measurements were acquired when the fluidic oscillator was fully submerged in water, since the hot-film probe cannot be used in NaI solution. The hot-film anemometry system consisted of a single-wire hot-film probe (TSI 1212-20 W) with TSI 1053B anemometer and TSI 1057 signal conditioner. The diameter and length of the hot-film wire were 50.8 μm and 1.02 mm, respectively. This hot-film probe was located 1 mm away from the oscillator exit, at approximately the same location where the microphone-tube sensor was located. Since the spectral characteristics of a signal can be obtained from raw voltage data, neither sensor was calibrated. However, the microphone-tube sensor raw voltage data also required signal conditioning (amplification and filtering) similar to the hot-film probe. Figure 5 presents a comparison of the frequency measurements of the fluidic oscillator with both measurement systems. Even though the bandwidth of the microphone sensor (30–15,000 Hz) was limited on the low end relative to the frequencies measured here, the measurements agreed well and showed that the microphone-tube sensor is capable of measuring the frequency of the fluidic oscillator accurately. Furthermore, both sensors captured the oscillation mechanism change occurring around 4 mL/s.

2.4 Quarter period-based method for PIV phase-averaging

The feedback-free fluidic oscillator creates an oscillating jet in a periodic manner. An important step to extract the internal flow field of the oscillator with the PIV technique is to phase-average the velocity fields throughout one period of the oscillation. However, unavoidable flow rate fluctuations complicated the PIV phase-averaging. The flow rate fluctuations in this study were approximately 1 %, leading to concomitant frequency fluctuations as high as 5 % since the frequency of the oscillator depends on the flow rate. To determine the cause of these fluctuations, the flow meter was removed from the main supply line and connected to one of the inlets of the fluidic oscillator to monitor the spectral properties of the signal at one of the inlets. The frequency of the oscillator was found to be measurable from the flow meter signal; however, the peak amplitude was very low and the peak dropped out intermittently. This indicates that not only the pumping system is the cause of the flow rate fluctuations, but the fluidic oscillator itself also has an effect on the fluctuations. Therefore, fluctuations were observed to occur due to the unsteady flow field and a non-ideal fluid supply system. The microphone-tube signal showed a continuously varying amplitude and period due to these fluctuations. Furthermore, even quarter periods were different from one another within a single period. A review of literature indicated that many phase-averaging methods were employed to address turbulent flows and periodic unsteady flows. Alfredsson and Johansson (1984) described some phase-averaging methods such as visual, band-pass filtering, short-time autocorrelation, pattern recognition, and various variable-interval time-averaging (VITA) techniques based on u velocity, v velocity or temperature. These are based on evaluation of the probe signal and were used especially in turbulence production to detect the frequency of occurrence of bursting. Furthermore, phase-averaging can also be obtained by conditional sampling, frequency filtering, and cycle-by-cycle smoothing, with these methods mainly being used to decompose a measured time-varying signal into a mean part and a fluctuating part in periodic unsteady flows (Wernert and Favier 1999).

The phase-averaging difficulties due to the flow rate fluctuations can be further illustrated by using the recorded microphone-tube signal presented in Fig. 6 (sampling rate of 5 kHz). In this plot, 0.1 s of the amplified and filtered signal is presented. Both the amplitude and period of the signal vary with time. In order to discuss period variations, one period from Fig. 6, marked with the rectangle, was selected and presented in Fig. 7. In this figure, the peak amplitude of the positive half of the period ($A1+$) is 1.193 V, and the peak amplitude of the negative half ($A2-$)

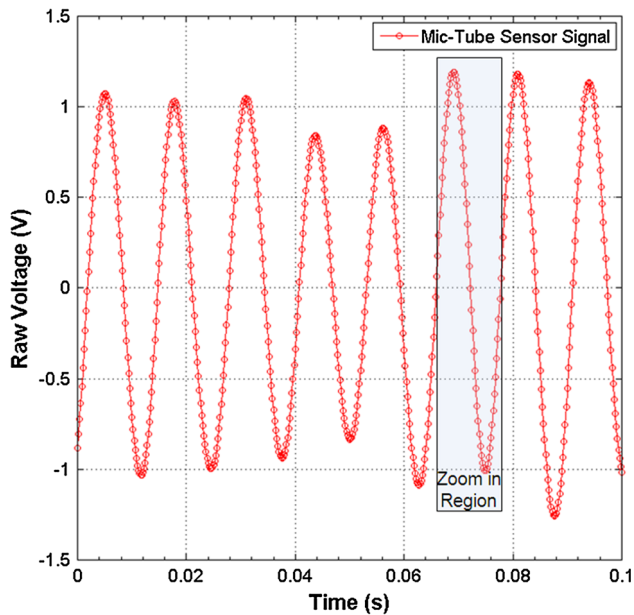


Fig. 6 Sample microphone-tube recording

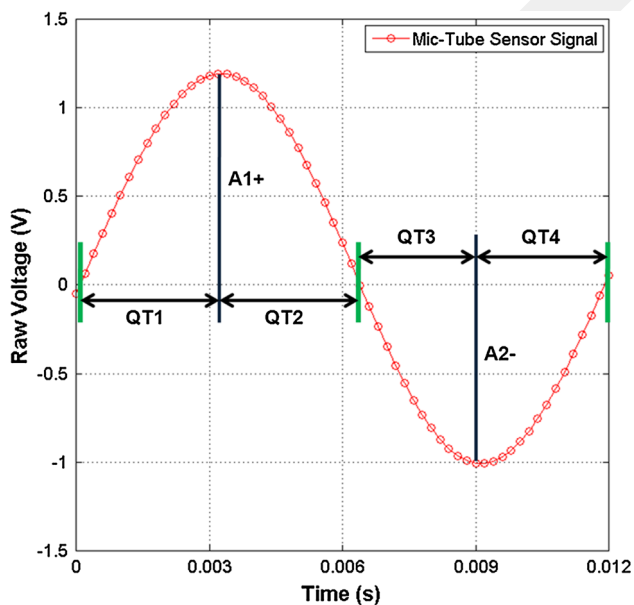


Fig. 7 Sample cycle from recorded microphone-tube data (zoomed-in image of highlighted *rectangular* region in Fig. 6)

is -1.006 V. First of all, $A1+$ is higher than $A2-$ which clearly indicated amplitude variations. Secondly, quarter period 4 (QT4), valued at 0.0029 s, for instance, is longer than quarter period 3 (QT3), valued at 0.0026 s. Furthermore, the positive-half period (QT1 + QT2), valued at $0.0033 + 0.0032$ s, is longer than the negative-half period (QT3 + QT4). Therefore, observations of the recorded

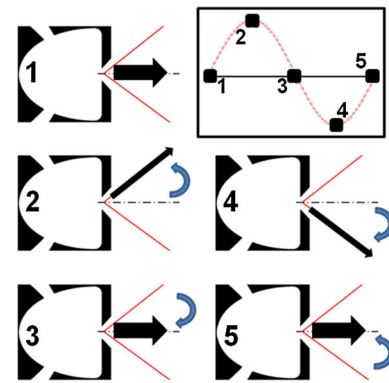


Fig. 8 Exiting jet flow direction changing points on fluidic oscillator in one period of recorded microphone-tube sensor signal

microphone-tube data indicated that the flow rate, and thus frequency fluctuations were continuous (even in a single cycle) and unpredictable; this complicated any phase-locking method.

A quarter period-based method for phase-averaging is mainly based on the interpretation of the microphone-tube signal in quarter periods. Figure 8 shows a sample microphone-tube signal along with the flow direction of the exiting jet at each quarter period (1–2, 2–3, 3–4, and 4–5) depicted by the curved arrows. In this figure, black arrows represent the location where the exiting jet changes its flow direction relative to the exit centerline. These direction changes manifest themselves as peaks and zeroes in the microphone-tube data, as shown in the top right of the figure. This is true regardless of the amplitude or period value (i.e., peaks and zeroes indicate exiting jet flow direction changes). These peaks and zeroes are used as the reference points for the following approach. First of all, the microphone-tube sensor and the PIV camera trigger signals were recorded simultaneously. Each quarter was divided into 10 bins, and the quarters encompassing the camera trigger signals were extracted for all 600 PIV images. Second, the camera trigger signal's time distance to a reference point (i.e., a peak or a zero point) on its left side was divided by that quarter's time length to obtain the proportional delay of that image within the quarter period. If the quarter type (1–2, 2–3, 3–4, and 4–5 as shown in Fig. 8) of the images is the same and the proportional delay value of the images falls in the same bin, they were used to obtain phase-averaged values of that bin. By using this construction approach, a period was constructed from total number of 40 bins. This corresponded to 9° phase angle window for each bin, and for the experimented Re of 1,350, the average number of images in each bin was 15; the maximum number of images in a bin was 19 and minimum number of images was 10.

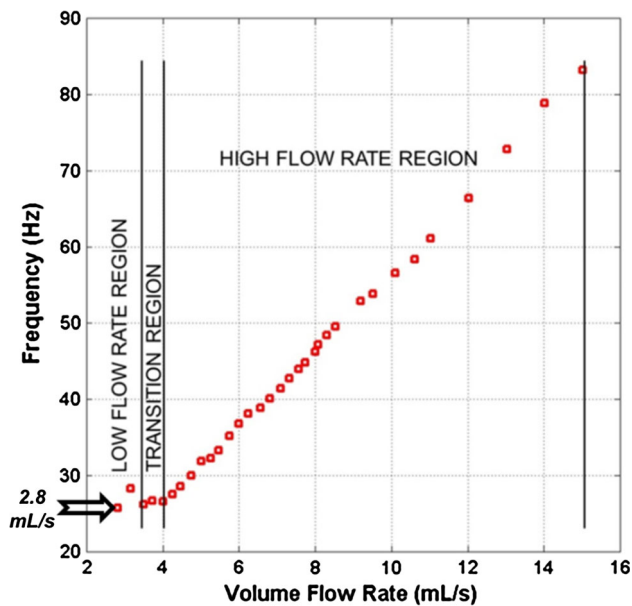


Fig. 9 Volume flow rate-frequency characteristics of the fluidic oscillator

3 Results

Tomac and Gregory (2012) reported the existence of three flow rate regions when the frequency characteristics of the fluidic oscillator were examined. Borders of these regions for the tested fluidic oscillator are provided in Fig. 9 for the flow rates from 2.8 to 15 mL/s. The presented results belong to the flow rate of 2.8 mL/s, and this flow rate corresponds to Re number of 1,350 calculated based on the exit nozzle width (2 mm), average velocity at the exit nozzle (0.935 m/s), and the kinematic viscosity of NaI solution at 28.9 °C ($1.382 \times 10^{-6} \text{ m}^2/\text{s}$). The results and discussion presented here illuminate the unknown flow physics and oscillation mechanism of the feedback-free fluidic oscillator in the low flow rate region and provides useful information on dual jet interactions and bifurcations, the role of the side and dome vortices in the oscillation mechanism, the interaction of the walls with the jets, and the vortices in the low flow rate region.

Figure 10 represents instantaneous vorticity contours with superimposed streamlines at an arbitrary phase in the oscillation cycle. The image shows the characteristic flow features that form inside the fluidic oscillator throughout the oscillation process. Two jets issue into the interaction chamber: the upper jet creates two shear layers (1, 2) and the lower jet creates two additional shear layers (3, 4). The upper jet right shear layer (2) feeds the upper side vortex (6) and the upper jet left shear layer (1) feeds the upper dome vortex (7). Likewise, the lower jet right shear layer (4) feeds the lower side vortex (5) and the lower jet left

shear layer (3) feeds the lower dome vortex which does not exist for this phase, but it forms in the other half period of the oscillation. Vortices in the dome region form and vanish depending on the phase; however, the side vortices just change size, shape, and strength but never vanish. The bifurcated branch of lower jet coalesces with the upper jet through the dome region (10), and an indicator of the bifurcation process is the saddle point (8) created inside the fluidic oscillator. Eventually, due to the interaction of all these flow features, an unsteady oscillating exiting jet (9) is created at the exit of the fluidic oscillator.

Figure 11 shows the streamlines superimposed onto the velocity contours (left) and vorticity contours (right) at 0° phase angle. 0° phase angle represents the average of the velocity fields that fell into the phase bin between 0° and 9°. In the vorticity plots, blue colors denote vorticity of a clockwise sense while the red colors signify vorticity of a counterclockwise sense. For this instant, the upper jet's core is connected with the exiting jet, and most of the kinetic energy that the upper jet has is transferred to the exiting jet. At this time, the upper jet's right shear layer is not energizing the upper side vortex as most of the kinetic energy is being transferred to the exiting jet. On the other hand, the core of the lower jet is not extending up to the exiting jet and the lower jet is bifurcated into two parts. The right branch, formed by the lower jet's right shear layer, is deflected by the upper jet and energizes the lower side vortex while the left branch of the lower jet coalesces with the upper jet via the dome region while suppressing the upper jet's left shear layer and adding some of the kinetic energy from the lower jet to the upper jet (this is why the upper jet core can extend to the exiting jet while that of the lower jet cannot). Furthermore, the upper jet is continuously bended by the lower jet's left branch over a half cycle of the oscillation with one such instance seen in Fig. 11. Therefore, the coalescence process bends the upper jet and also adds kinetic energy to the upper jet, but does not cut the upper jet's core connection with the exiting jet. Nevertheless, the lower jet's left shear layer starts creating a small dome vortex as shown with a white arrow in the velocity contour plot. This small dome vortex starts entraining some portion of the left branch of the lower jet while squeezing and pushing the rest toward the upper jet as it grows. Therefore, when the lower jet's right shear layer energizes the lower side vortex, it becomes strong enough to push the lower jet toward the dome region, and this push causes the lower jet's left shear layer to start creating a dome vortex which entrains some portion of the lower jet toward the dome region. As seen in the vorticity contours, the vorticity involved with the lower side vortex is higher than the upper side vortex, and so the size of the vortex is relatively bigger such that it pushes the lower jet toward the dome region and lower jet reacts to this push by

Fig. 10 Nomenclature for internal flow features

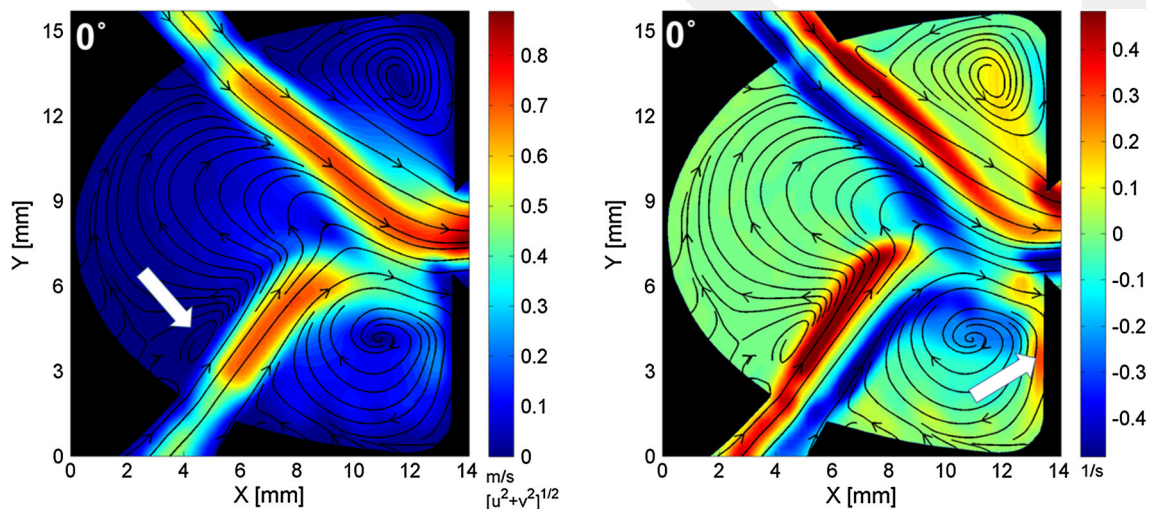
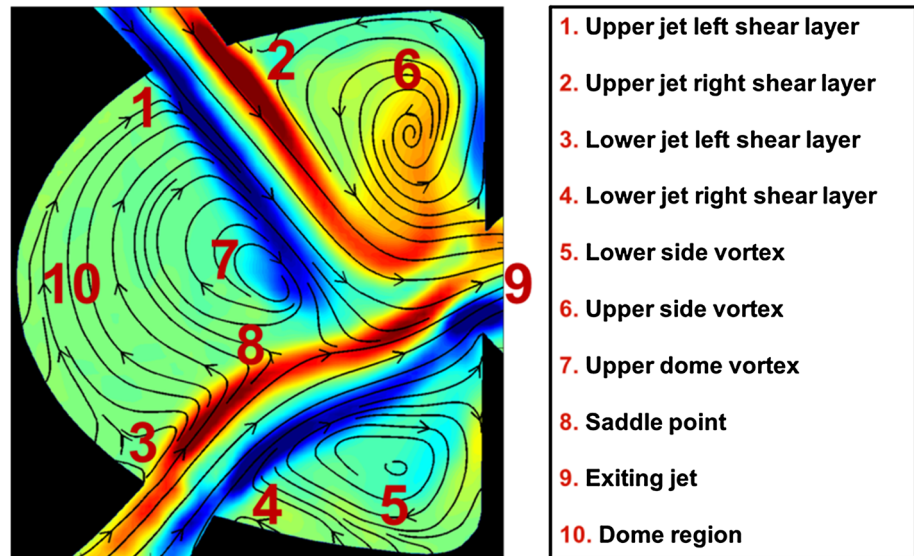


Fig. 11 Streamlines superimposed on velocity (*left*) and vorticity (*right*) contours at 0° phase angle ($Re = 1,350$)

creating the dome vortex. In fact, the vorticity attributed to the upper side vortex is a remnant from the previously energized upper side vortex caused by the bending of the upper jet in another phase of the oscillation where the lower jet's core had been fully connected with the exiting jet. This will be shown in subsequent phase results. Also, the increase in vorticity at the two lips of the exit is due to the sharp edges of the orifice and shows the shear layers of the exiting jet. Furthermore, the lower side vortex increases the vorticity of opposite sign in the boundary layer formed on the wall at the bottom part of the oscillator's exit, as shown by the white arrow in the vorticity plot. A similar effect but with less vorticity change is also observable in the vicinity of the upper side vortex over the wall.

Figure 12 presents the velocity and vorticity contours for a phase angle of 45° . The data demonstrate that as the

dome vortex is fed by the lower jet's left shear layer, the size of the dome vortex grows. More important is the observation that the dome vortex moved increasingly farther away from the dome wall toward the upper jet. As the dome vortex becomes stronger and larger, it starts pushing the lower jet toward the exit and constricting the left bifurcated branch of the lower jet in the dome region between itself and the upper jet. The core of the lower jet extends closer to the exit, and the connecting region between the upper jet and exiting jet is reduced. Under the influence of the lower jet's motion toward the exiting jet, the lower side vortex migrates closer to the walls, which is followed by increased vorticity changes near the surface. On the other hand, the upper side vortex is very weak as shown in the velocity contours with mostly dark regions indicating velocities near zero. The reason for that is this

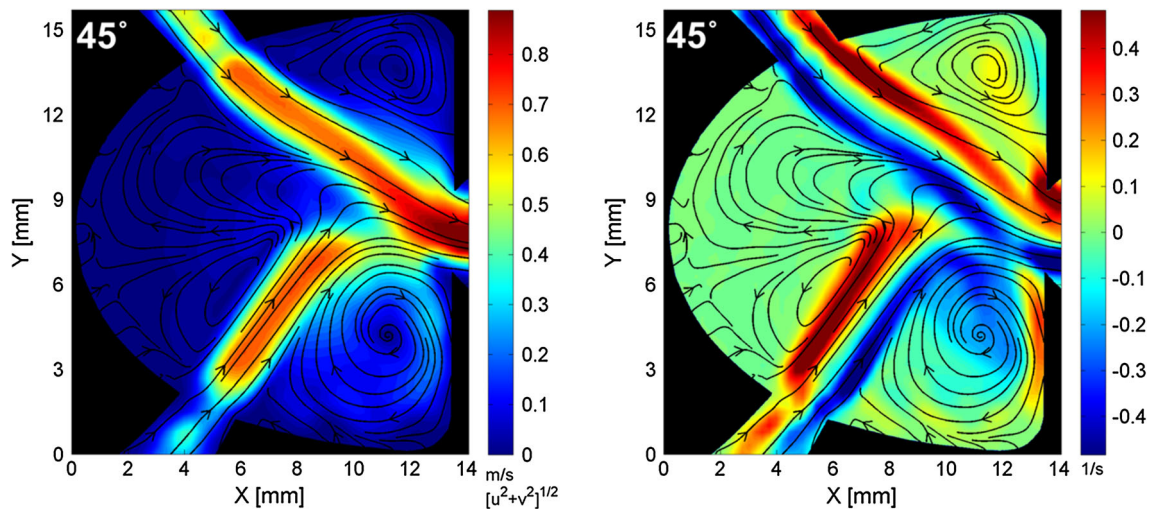


Fig. 12 Streamlines superimposed on velocity (*left*) and vorticity (*right*) contours at 45° phase angle ($Re = 1,350$)

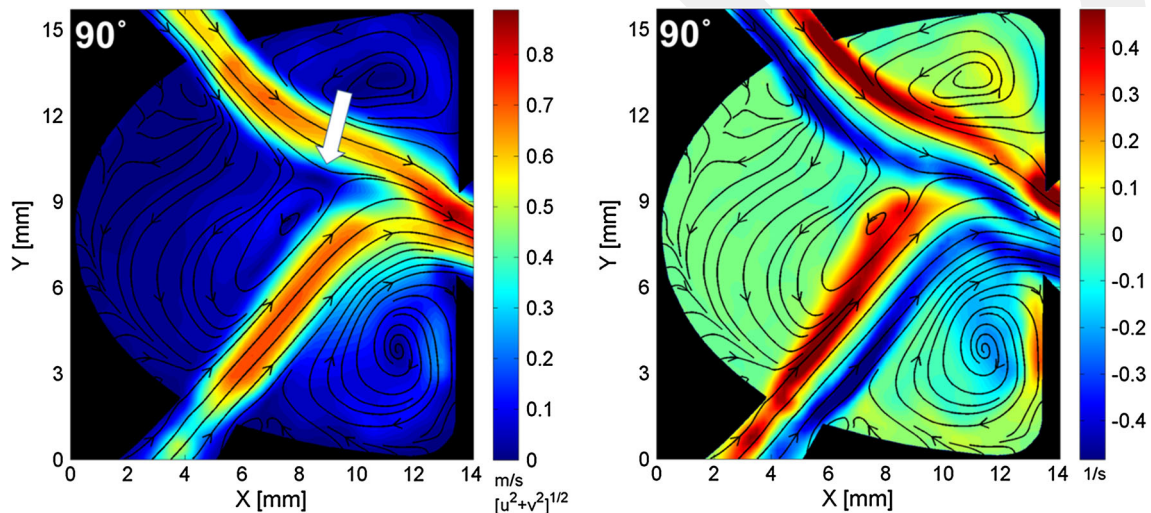


Fig. 13 Streamlines superimposed on velocity (*left*) and vorticity (*right*) contours at 90° phase angle ($Re = 1,350$)

side vortex is not energized by any of the jets, and so its kinetic energy is diminished due to the viscous effects and some of the energy is transferred to the exiting jet via the vorticity created by the sharp surfaces near the exit orifice.

As the dome vortex approaches the upper jet, as shown in Fig. 13, there is no room left for the lower jet's left branch to coalesce with the upper jet, so the dome vortex starts bifurcating the upper jet, and this time the left branch of the upper jet starts to coalesce with the lower jet in the dome interaction region. Furthermore, the potential core of the lower jet extends much closer to the exiting jet while the upper jet's core connection with the exiting jet continues to become thinner. At this very moment, a saddle point is clearly seen between the dome vortex and the upper jet, as marked with a white arrow in the velocity contours showing that the dome vortex reaches the upper

jet and starts bifurcating it. The strength of the lower side vortex decreased as seen in the vorticity contours, since the lower jet core gets closer to connect with the exiting jet (i.e., it is about to stop energizing the lower side vortex).

Figure 14 shows one of the major findings of this study. In this figure, the dome vortex and the saddle point are shown to collide, and this collision cuts the connection of the upper jet's potential core with the exiting jet while the lower jet's core starts connecting with the exiting jet. Therefore, this collision between the dome vortex and the saddle point was discovered as the underlying mechanism of the jet-switching behavior. As shown in the velocity contours of Fig. 14, the upper jet's core region is no longer connected with the exiting jet while the lower jet becomes the internal jet which feeds the exiting jet.

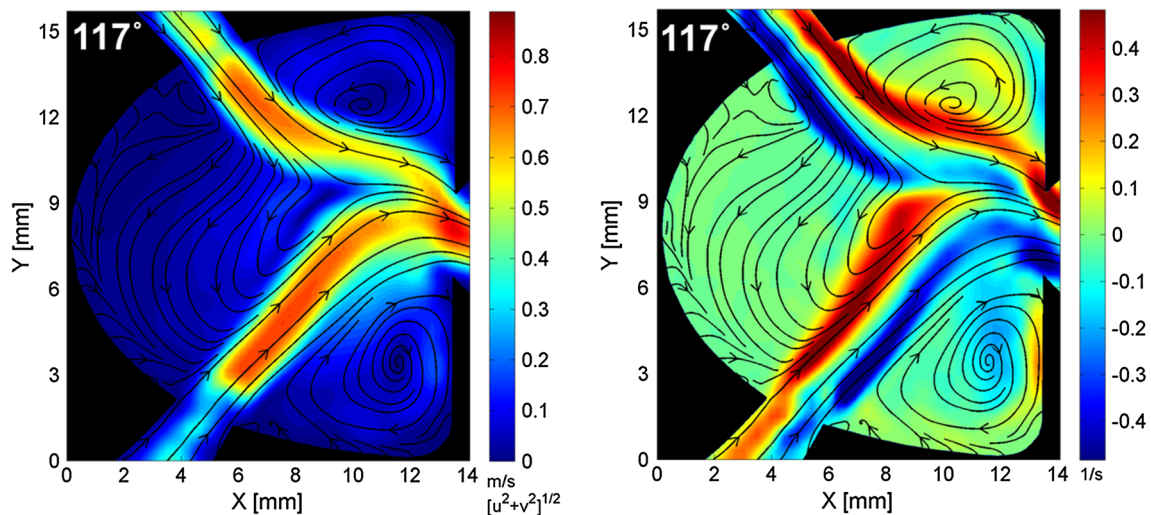


Fig. 14 Streamlines superimposed on velocity (left) and vorticity (right) contours at 117° phase angle ($Re = 1,350$)

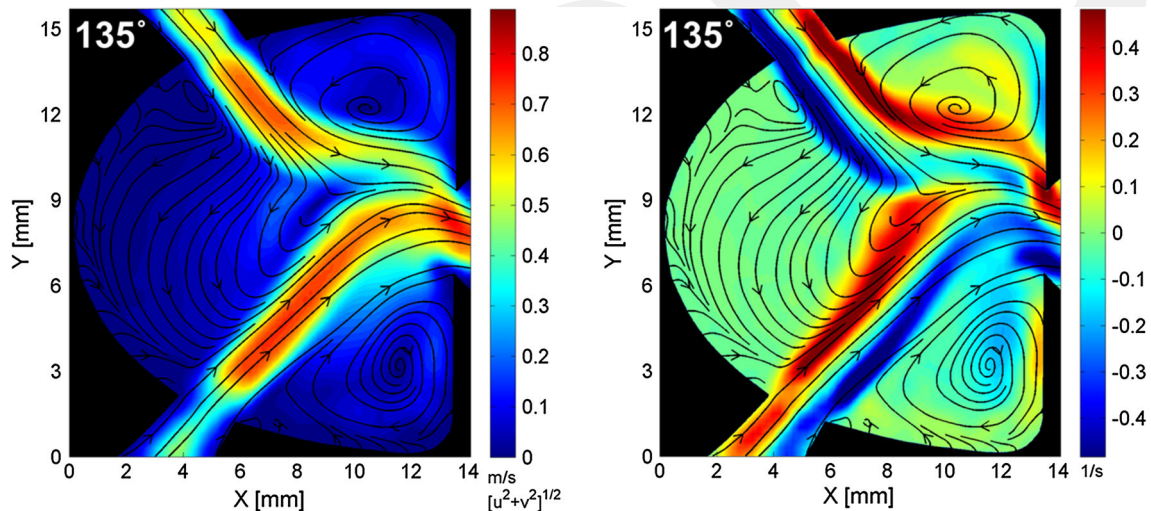


Fig. 15 Streamlines superimposed on velocity (left) and vorticity (right) contours at 135° phase angle ($Re = 1,350$)

For the 135° phase angle as shown in Fig. 15, the upper side vortex is beginning to be energized by the bended upper jet's right shear layer. However, the upper jet is still not deflected toward the upper side vortex region and is still connected with the exiting jet. The vorticity in the wall boundary layer in the vicinity of upper side is increased. A small dome vortex is formed by the upper jet's left shear layer, similar to the one created by the lower jet's left shear layer at the beginning of the oscillation cycle.

At a phase angle of 180°, half of the oscillation period is completed as seen in Fig. 16. A dome vortex fed by the upper jet's left shear layer is growing stronger and larger while the upper jet's right shear layer is deflected toward the upper side vortex which is being energized by this shear

layer. At this time, the potential core of the lower jet is connected with the exiting jet. Also, although the upper jet is not cut off from colliding with the lower jet, the core of the upper jet is not connected with the exiting jet.

A half period of the oscillation in the low flow rate region is completed with the phase angle of 180°. The rest of the oscillation period has a similar mechanism; however, the role of the jets, shear layers, and vortices are switched. The other half period is shown in Figs. 17, 18, 19 and 20. When these figures are considered, it was observed that neither of the jet shear layers (lower jet or upper jet) can extend beyond the exit centerline at the same time. Figure 17 shows the velocity and vorticity contours with the streamlines superimposed for a phase angle of 225° in

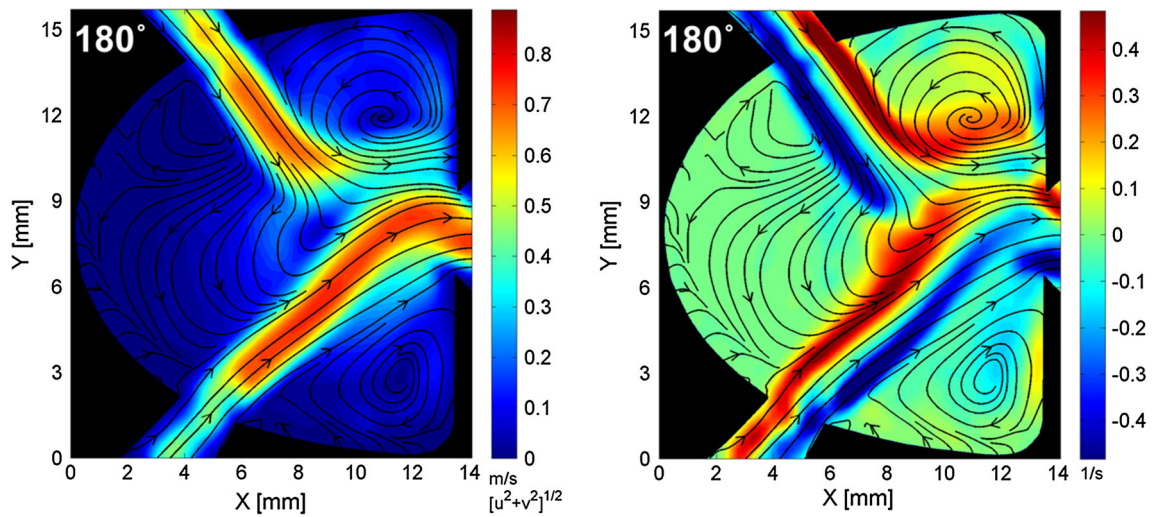


Fig. 16 Streamlines superimposed on velocity (*left*) and vorticity (*right*) contours at 180° phase angle ($Re = 1,350$)

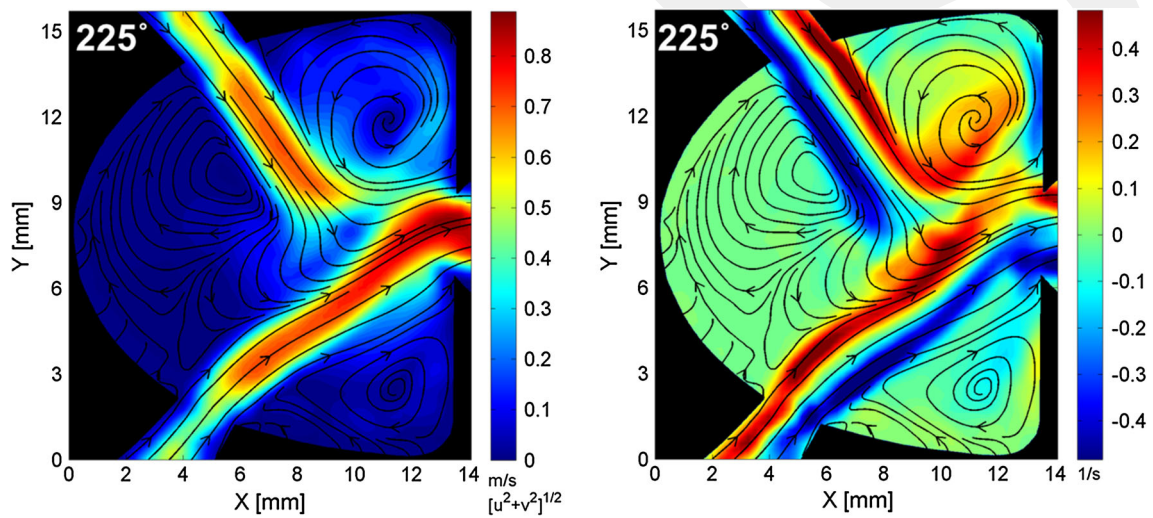


Fig. 17 Streamlines superimposed on velocity (*left*) and vorticity (*right*) contours at 225° phase angle ($Re = 1,350$)

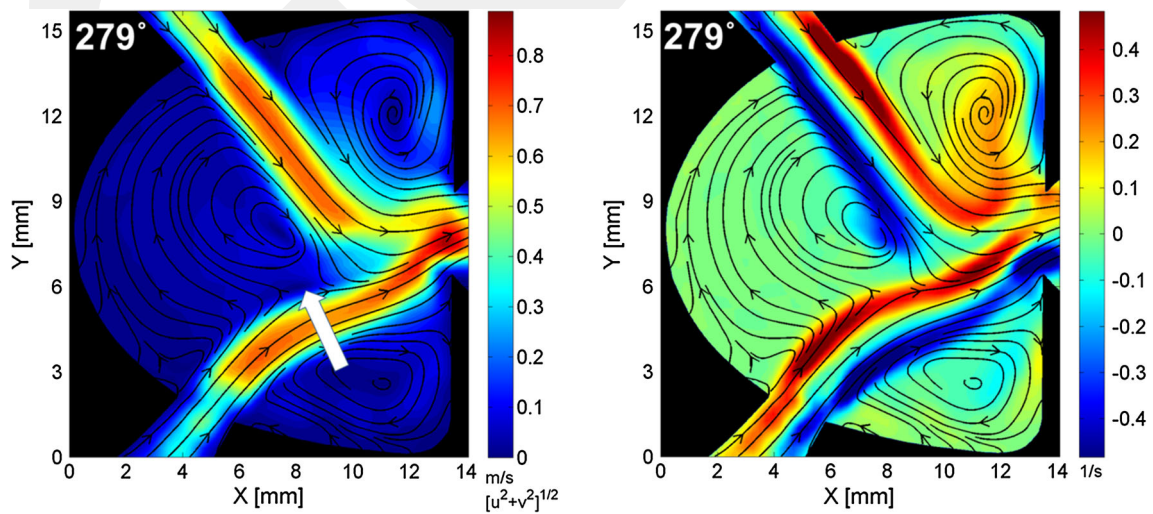


Fig. 18 Streamlines superimposed on velocity (*left*) and vorticity (*right*) contours at 279° phase angle ($Re = 1,350$)

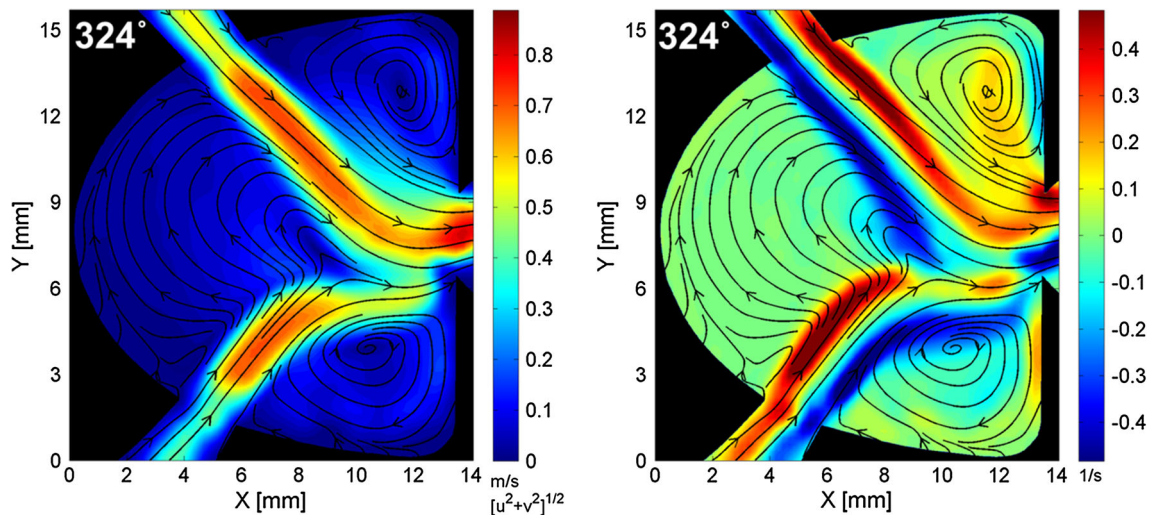


Fig. 19 Streamlines superimposed on velocity (left) and vorticity (right) contours at 324° phase angle ($Re = 1,350$)

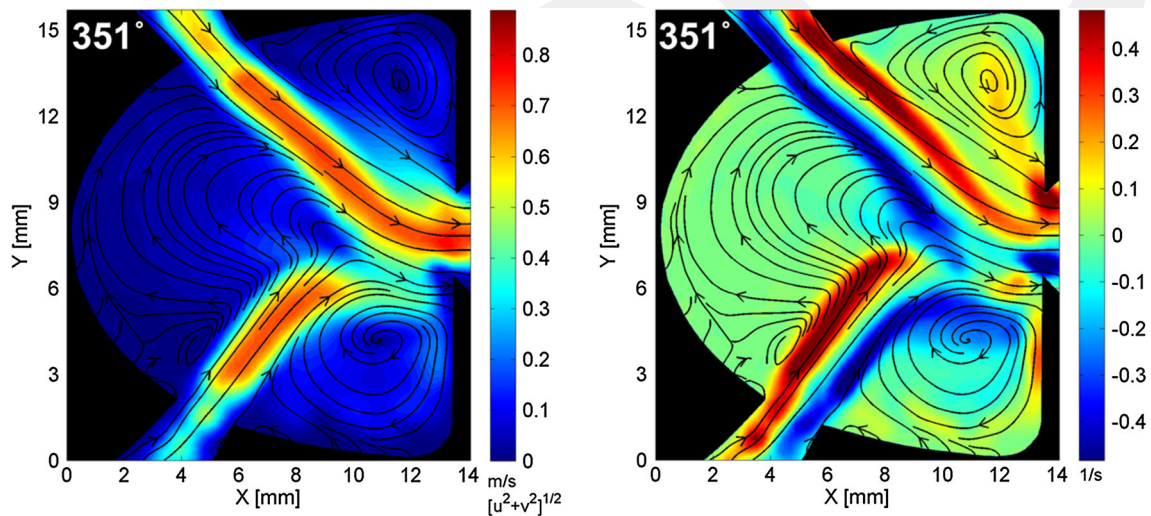


Fig. 20 Streamlines superimposed on velocity (left) and vorticity (right) contours at 351° phase angle ($Re = 1,350$)

the low flow rate region. Similar to the first half of the oscillation period, the dome vortex created by the upper jet's left shear layer is moving toward the lower jet while it constricts the left branch of the upper jet between itself and the lower jet. For the phase angle of 279° shown in Fig. 18, the lower jet is now bifurcated, and it coalesces with upper jet over the dome vortex while the saddle point is clearly seen and shown with a white arrow on the left image. In Fig. 19, collision of the dome vortex and the saddle point has been completed, and the potential core of lower jet is no longer connected to the exiting jet any longer, but the upper jet core is now connected to exiting jet. Finally, for the phase angle of 351° shown in Fig. 20, the upper jet core is connected with the exiting jet, signifying that the lower







jet has been bifurcated; the left branch coalesces with the upper jet, and the right branch is deflected to energize the lower side vortex.

Jet interactions and oscillation mechanism of a feedback-free fluidic oscillator at low flow rate are discussed in this section in detail. Table 1 summarizes the main flow physics for each phase angle in the first half of the oscillation with the help of the flow streamlines.

4 Conclusion

In this study, the internal jet interactions and oscillation mechanism of a feedback-free fluidic oscillator in the low

Table 1 Summary of main flow physics for the first half of the oscillation

Phase angle (°)	Streamlines	Summary of main flow physics
0		Upper jet's core is connected to the exiting jet while the lower jet is bifurcated Dome region branch of the bifurcated lower jet transfers its kinetic energy to the upper jet A small lower dome vortex is created by the lower jet left shear layer Lower side vortex is larger and stronger than the upper side vortex
45		Size of the lower dome vortex grows as it is fed by the lower jet left shear layer As the lower dome vortex grows, it moves toward the upper jet and constricts the bifurcated branch of the lower jet in the dome region between itself and the upper jet
90		Lower dome vortex reaches the upper jet and starts bifurcating it A saddle point is formed and indicates that the jet bifurcation process is taking place The bifurcation process changes the flow direction in the dome region from the upper jet to the lower jet in contrast to the previous phase angle
117		Lower dome vortex collides with the saddle point, and the saddle point disappears indicating that the lower dome vortex had burst The upper jet is still bifurcated and transferring some of its kinetic energy to the lower jet The core of the upper jet is no longer connected to the exiting jet
135		The lower jet's core is connected to the exiting jet This time, a small dome vortex is being created by the upper jet The upper jet is still bifurcated and transferring some of its kinetic energy to the lower jet
180		Half of the oscillation is completed Upper dome vortex is growing stronger and larger The core of the lower jet is still connected to the exiting jet Upper side vortex is larger and stronger than the lower side vortex

flow rate region were extracted by using a refractive index-matched PIV technique along with a custom made microphone-tube sensor configuration, and a quarter period-based PIV phase-averaging method. It was observed that two jets continuously collide with each other in the low flow rate region; however, jet bifurcation still takes place as the main kinetic energy transfer method between the jets. Phase-averaged PIV results also showed the existence of four main vortices (two dome and two side vortices) created by the shear layers of the two jets. Dome vortices were found to be mainly responsible for the jet bifurcation, and they were observed to appear and vanish throughout the period. Nevertheless, side vortices never vanished; instead, they exhibited continuous changes in size, shape, and strength. While the side vortices went through these changes, they trigger the creation of the dome vortices, push the jets to change their flow direction at the exit, and increase the vorticity of negative sign over the walls. Oscillatory behavior in the low flow rate region is a result of many interesting fluid mechanics phenomena such as jet interactions and bifurcations, vortex–shear layer interactions, vortex–wall interactions, and saddle point formations.

References

- Alfredsson HP, Johansson AV (1984) Time scales in turbulent channel flow. *Phys Fluids* 27(8):1974–1981
- Bidadi S, Heister SD, Matsutomi Y (2011) Computational and experimental study of jet interaction fluidic injectors. *At Spray* 21(2):127–138
- Bobusch BC, Wozidlo R, Bergada JM, Nayeri CN, Paschereit CO (2013) Experimental study of the internal flow structures inside a fluidic oscillator. *Exp Fluids* 54:1559
- Booth WA (1962) Performance evaluation of a high-pressure-recovery bistable fluid amplifier. In: *Fluid jet control devices, proceedings of the symposium on fluid jet control devices at the winter annual meeting of the ASME, New York*, pp 83–90
- Budwig R (1994) Refractive index matching methods for liquid flow investigations. *Exp Fluids* 17:350–355
- Denshchikov VA, Kondrat'ev VN, Romashov AN (1978) Interaction between two opposed jets. *Fluid Dyn* 13(6):924–926. doi:10.1007/BF01050971
- Gaylord W, Carter V (1969) *Fluerics 27: flueric temperature-sensing oscillator design*, Harry Diamond Laboratories, Washington, DC, HDL TR-1428, DTIC accession number AD0689444
- Gregory JW, Tomac MN (2013) A review of fluidic oscillator development and application for flow control. In: *AIAA-2013-2474, 43rd AIAA fluid dynamics conference*, San Diego, CA
- Gregory JW, Sullivan JP, Raghu S (2005) Visualization of jet mixing in a fluidic oscillator. *J Vis* 8(2):169–176
- Gregory JW, Sullivan JP, Raman G, Raghu S (2007) Characterization of the microfluidic oscillator. *AIAA J* 45(3):568–576
- Lush PA (1968) A theoretical and experimental investigation of the switching mechanism in a wall attachment fluid amplifier. In: *Proceedings IFAC symposium on fluidics*, paper A3
- Raghu S (2001) *Feedback-free fluidic oscillator and method*. U.S. Patent 6,253,782, issued July 3, 2001

- Raghu S (2013) Fluidic oscillators for flow control. *Exp Fluids* 54:1455
- Spyropoulos CE (1964) A sonic oscillator. In: Proceedings of the fluid amplification symposium, vol III, 1964, pp 27–52
- Srinath DN, Koehler E (2001) Nozzles with integrated or built-in filters and method. US Patent 6,186,409, issued February 13, 2001
- Tesař V, Bandalusena HCH (2011) Bistable diverter valve in microfluidics. *Exp Fluids* 50:1225
- Tesař V, Zhong S, Rasheed F (2013) New fluidic-oscillator concept for flow-separation control. *AIAA J* 51(2):397–405. doi:[10.2514/1.J051791](https://doi.org/10.2514/1.J051791)
- Tomac MN, Gregory JW (2012) Frequency studies and scaling effects of jet interaction in a feedback-free fluidic oscillator. In: AIAA 2012-1248, 50th AIAA Aerospace Sciences Meeting, Nashville, TN
- Tomac MN, Gregory JW (2013) Jet interactions in a feedback-free fluidic oscillator at low flow rate region. In: AIAA 2013-2478, 43rd AIAA fluid dynamics conference and exhibit, San Diego, CA
- Uzol O, Chow Y-C, Katz J, Meneveau C (2002) Unobstructed particle image velocimetry measurements within an axial turbo-pump using liquid and blades with matched refractive indices. *Exp Fluids* 33:909–919
- Wernert P, Favier D (1999) Considerations about the phase averaging method with application to ELDV and PIV measurements over pitching airfoils. *Exp Fluids* 27:473–483
- Zaytsev ID, Aseyev MA (1992) Properties of aqueous solutions of electrolyte. CRC Press, Boca Raton